ORIGINAL PAPER

High-Temperature Corrosion of Chromia-Forming Ni-Based Alloys in CO$_2$ Containing Impurities

Richard P. Oleksak[1] · Joseph H. Tylczak[1] · Lucas Teeter[1,2] · Casey S. Carney[1,2] · Ömer N. Doğan[1]

Abstract

Future technologies require structural materials resistant to environmental degradation in high-temperature CO$_2$-rich environments. Herein, we exposed several commercially available Ni-based alloys (230, 263, 282, 617, 625, and 740H) to atmospheric pressure gases intended to simulate the compositions expected in future direct-fired supercritical CO$_2$ power cycles. The alloys were exposed to 95% CO$_2$ + 4% H$_2$O + 1% O$_2$ and the same gas containing 0.1% SO$_2$ at temperatures of 600, 650, 700, 750, and 800 °C for 2500 h. With minor exceptions, chromia scales formed on all alloys at all temperatures in the SO$_2$-free gas, yielding parabolic growth rates that followed an Arrhenius temperature dependence. Behavior in the SO$_2$-containing gas was more complex. Generally, the alloys performed well at temperatures of 650, 750, and 800 °C. While some alloys further performed relatively well across the whole temperature range, several of the alloys experienced chromia failure resulting in non-protective duplex oxide scales and high oxidation rates, at temperatures of 600 and 700 °C. Deviation from protective behavior was associated with internal sulfide formation and, additionally for the case of 600 °C, external sulfate formation. Extensive carburization accompanied growth of the non-protective duplex oxide scales, which made it more difficult for the alloy to recover after initiation of the sulfur-induced accelerated corrosion process. The thermodynamic and kinetic factors influencing the accelerated corrosion in the presence of sulfur are discussed. The results suggest that caution is required when assessing compatibility of Ni-based alloys for CO$_2$-based systems when sulfur-based impurities are expected.

Keywords Direct-fired supercritical CO$_2$ power cycle · Ni-based superalloys · Oxidation · Sulfidation · Carburization

✉ Richard P. Oleksak
Richard.Oleksak@netl.doe.gov

1 National Energy Technology Laboratory, 1450 Queen Ave SW, Albany, OR 97321, USA

2 NETL Support Contractor, 1450 Queen Ave SW, Albany, OR 97321, USA

Introduction

Supercritical carbon dioxide (sCO_2) power cycles offer the potential for high conversion efficiencies, compact size, and other benefits in next-generation power plants [1]. The cycles can be generally separated into two categories. Indirect sCO_2 cycles rely on a closed loop of pure sCO_2 as the working fluid. Due to the general nature of the heat input, indirect sCO_2 cycles are amenable to virtually any energy source including fossil, nuclear, concentrated solar, geothermal, etc. Alternatively, direct (a.k.a. direct-fired) sCO_2 cycles, such as the NET Power cycle [2], are specific to fossil fuels as an energy source, as the CO_2-rich stream produced by oxy-combustion of the fuel is itself used as the working fluid of the cycle. A major benefit of this cycle is that sequestration-ready CO_2 is produced as a byproduct, thus enabling built-in carbon capture. Unlike the indirect configuration, direct sCO_2 cycles rely on a semi-open loop of sCO_2 containing relatively high (1–10%) levels of H_2O and/or O_2 impurities associated with the oxy-combustion process, while additional (e.g., sulfur-based) impurities may also be present depending on the fuel.

One of the primary barriers to realizing sCO_2 power cycle technology is identifying materials that can endure the extreme conditions expected in these systems. Specifically, turbine outlet temperatures on the order of 800 °C are desired to achieve high efficiencies. This necessitates alloys capable of withstanding environmental degradation in hot CO_2-rich environments to be used as heat exchangers up to these temperatures. Due to prior research efforts to enable other technologies such as gas-cooled nuclear reactors, oxyfuel combustion systems, and solid oxide fuel cells, in addition to more recent efforts in support of sCO_2 power cycles, the oxidation performance of different classes of alloy in pure CO_2 and sCO_2 up to these temperatures is now relatively well understood [3]. In particular, Ni–Cr based alloys, which are needed for sCO_2 systems at temperatures exceeding about 600 °C (where the creep strength of steels becomes unacceptable), perform well in these environments, almost universally forming slow-growing chromia scales during long-term exposures [4, 5] and carburizing only at low rates [4]. Alternatively, the oxidation performance of Ni-based alloys in the impure CO_2-rich environments relevant to direct sCO_2 cycles is less understood. The effects of O_2 and H_2O impurities, ranging from approximately 0.01 to 10%, have been shown to impact the oxidation behavior of various Ni-based alloys in CO_2 and sCO_2, but generally have not revealed much cause for concern [6–15]. That is, oxidation rates do not deviate significantly from those expected for protective chromia scale growth, and carburization rates are likewise very low [16]. One notable exception is that water vapor-assisted chromia volatilization may become problematic at the high flow rates expected in real sCO_2 cycles when significant H_2O and O_2 impurities are present [16]. Alternatively, the limited available work has shown that sulfur-based impurities in the CO_2, while relatively innocuous in some cases [7, 17], can significantly degrade the oxidation performance in others [8, 18]. More generally, the unique corrosion concerns posed by high-temperature environments containing sulfur have long been recognized for alloys

generally [19–22] and Ni-based alloys specifically [23, 24]. This highlights the need to understand potential effects of sulfur impurities in these CO_2 based power systems.

The purpose of this study is to produce an improved understanding of the oxidation performance of various commercially available Ni-based alloys to inform materials selection for future power systems requiring durability in hot impure CO_2 environments. Specifically, the temperature dependence of oxidation is assessed over the temperature range currently envisioned for Ni-based alloys in direct sCO_2 cycles, in environments meant to simulate the compositions expected in these cycles, namely 95% CO_2, 4% H_2O, 1% O_2 with and without 0.1% SO_2. Due to experimental limitations related to high-pressure exposures involving sulfur compounds, the alloys were exposed to atmospheric pressure gases. Nevertheless, the results offer important insights into the potential degradation processes that should be considered when selecting Ni-based alloys for direct sCO_2 cycles and related applications.

Experimental Procedures

Plates of the commercially available Ni-based alloys were obtained from various manufacturers in the service-ready condition. Table 1 summarizes the alloy compositions.

Rectangular samples approximately 19 mm × 13 mm with thickness ranging from 0.4 to 2.0 mm were machined from the plates, and a 5 mm hole was drilled near the top of the sample for hanging during exposure. The samples were surface-finished using 600 grit SiC paper (CAMI designation), dimensioned with calipers, cleaned in acetone and/or alcohol, weighed on a microbalance (0.01 mg precision), and loaded into a horizontal tube furnace. The samples were hung on a rack constructed from alloy 617. Most exposures consisted of 2–3 replicate samples per alloy; however, in a small number of cases only 1 sample was available. The furnace was sealed, heated to 80 °C, and purged for several hours using high purity (99.999%) CO_2 at a flow that provided a linear velocity of 5 cm/min. After purging, the furnace was

Table 1 Compositions (wt%) of commercial Ni-based alloys measured by X-ray fluorescence (metallic elements) and combustion analysis (carbon)

Alloy	Ni	Cr	Fe	Co	Mo	W	Al	Si	Ti	Mn	Nb	C (ppm)
282	58.4	19.2	0.1	10.2	8.4	–	1.3	0.04	2.1	0.1	0.02	600
263	51.1	19.9	0.01	20.0	5.6	–	0.4	0.28	2.1	0.5	0.1	560
230	60.4	21.3	0.4	0.3	1.2	14.8	0.4	0.45	0.01	0.4	0.04	903
625	61.0	21.4	4.4	0.1	8.4	–	0.2	0.35	0.3	0.1	3.3	181
617[a]	55.1	21.8	0.4	11.4	9.6	–	1.0	0.02	0.5	0.04	0.03	843
617[b]	53.3	22.4	1.1	11.5	9.6	–	1.1	0.06	0.3	0.05	–	900
740H	50.6	24.5	–	20.1	0.3	–	1.2	0.12	1.4	0.2	1.5	238

[a]Alloy 617 heat used for 700 °C, 750 °C, 800 °C exposures [b]Alloy 617 heat used for 600 °C, 650 °C exposures.

heated to the target exposure temperature at a rate of approximately 200 °C/h. Upon reaching the exposure temperature, the gas flow was switched to a CO_2/O_2 or $CO_2/O_2/SO_2$ mixture, and liquid water was injected into a heated section of the furnace upstream from the samples. The gas mixture was passed through a Pd/Rd catalyst mesh to promote equilibration of the gas, especially with respect to the reaction $SO_2 + 1/2 O_2 = SO_3$. The flows were controlled to achieve a final gas composition of 95% CO_2, 4% H_2O, 1% O_2, with/without 0.1% SO_2, at a linear velocity of 25 cm/min at the reaction temperature. After the exposure iteration was completed (usually 500 h), water injection was stopped, the gas switched back to high purity CO_2, the furnace turned down, and the samples cooled at an initial rate of ≈ 200 °C/h. The samples were removed from the furnace, weighed, and reloaded for continued exposure according to the above procedure until a total exposure time of 2500 h.

Select samples were electroplated with copper (to protect the oxide scale during subsequent processing), sectioned, hot mounted in conductive epoxy, and polished to a 1 μm diamond finish to prepare for cross-sectional analysis. The cross sections were analyzed by scanning electron microscopy (SEM) and energy-dispersive X-ray spectroscopy (EDS) using an FEI Inspect F50 SEM or a JEOL JSM-IT700HR SEM operating at 20 kV. Electron probe microanalysis (EPMA) was done using a JXA-8530FPlus HyperProbe. Glancing angle X-ray diffraction (XRD) analysis was done using a Rigaku D/Max 2200PC Ultima III using Cu Kα radiation. Thermodynamic modeling was done using the FactSage version 8.2 software package.

Results

Mass Change

Figure 1 shows the mass change behavior of all alloys and conditions. At 750 °C, all alloys showed relatively low mass gains and essentially no effect of SO_2. Similarly, at temperatures of 650 and 800 °C, only minimal differences are evident for exposures done with and without SO_2. Alternatively, a significant impact of SO_2 is seen for several of the alloys at 600 and 700 °C. At 600 °C, several of the alloys showed systematically higher, albeit overall low (<0.4 mg/cm^2) mass gains in SO_2 compared to the SO_2-free condition. More strikingly, one alloy, 617, showed mass gains in SO_2 approximately two orders of magnitude higher than the SO_2-free condition (Fig. 1b). At 700 °C, alloy 740H was the only alloy to exhibit similar behavior regardless of SO_2, whereas all other alloys showed signs of increased corrosion, reflected by significant scatter in the data and significant mass losses, indicating scale spallation, beginning at times between 500 and 1500 h. In particular, very large mass losses (>15 mg/cm^2) occurred for alloy 263.

Characterization of Sulfur-Free Exposures

Figure 2 shows cross-sectional SEM images of several of the alloys exposed to the SO_2-free condition at 700, 750, and 800 °C. Thin (<10 μm) chromia scales
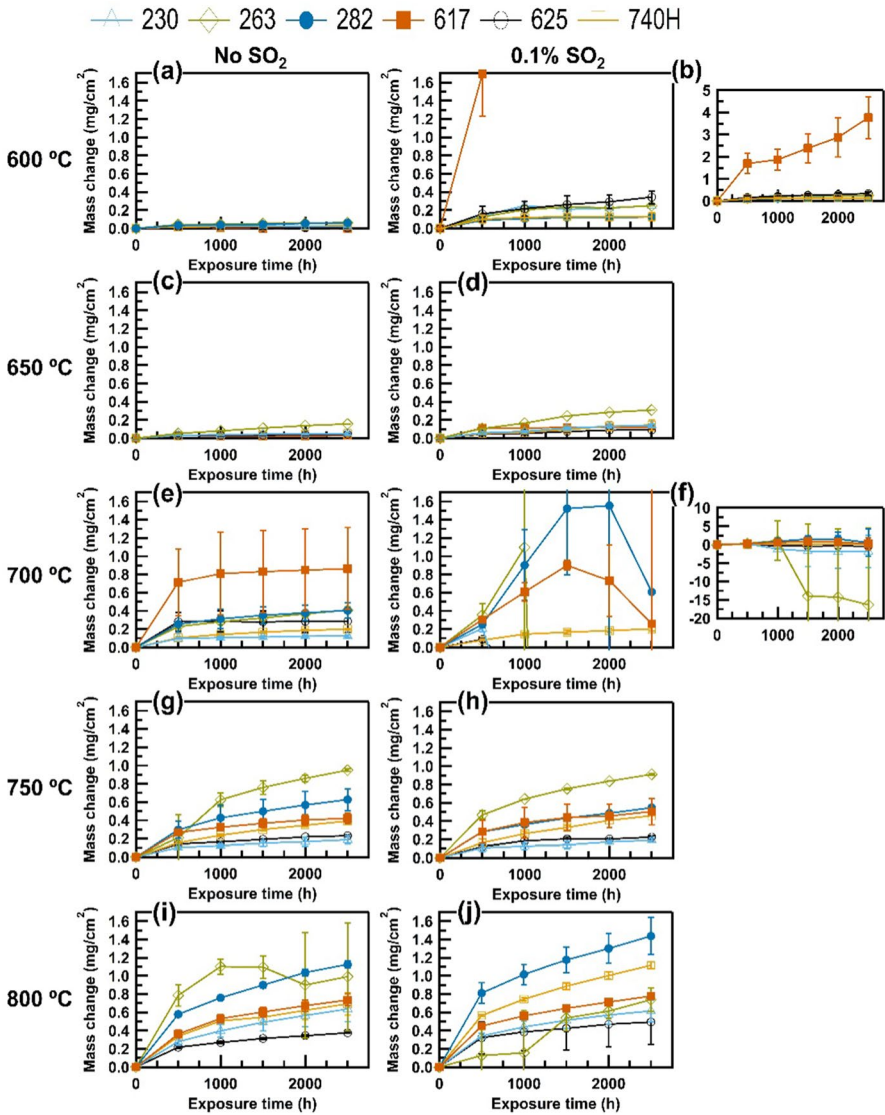
Fig. 1 Mass change of Ni-based alloys exposed to 1 bar of 95% CO_2 + 4% H_2O + 1% O_2 with and without 0.1% SO_2 at temperatures of **a, b** 600 °C, **c, d** 650 °C, **e, f** 700 °C, **g, h** 750 °C, **i, j** 800 °C

are observed in all cases, consistent with the low mass gains for all alloys and temperatures in SO_2-free exposures. Analysis of a typical chromia scale formed in the SO_2-free conditions is shown in Fig. 3, using alloy 263 at 750 °C as an example. In addition to the chromia scale, commonly observed features include internal oxidation of Al, Ti, and Si, as well as an outermost layer of Ti-oxide and Mn-rich spinel oxide, as described previously [6].
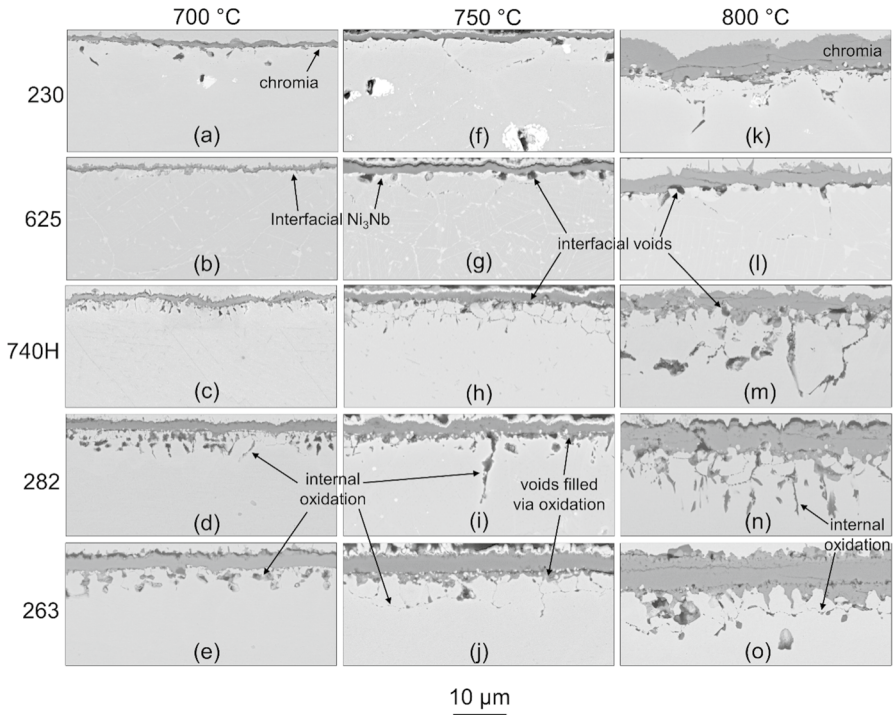
Fig. 2 Cross-sectional SEM images of various Ni-based alloys exposed for 2500 h to 1 bar of 95% $CO_2 + 4\%$ $H_2O + 1\%$ O_2 at temperatures of **a–e** 700 °C, **f–j** 750 °C, **k–o** 800 °C
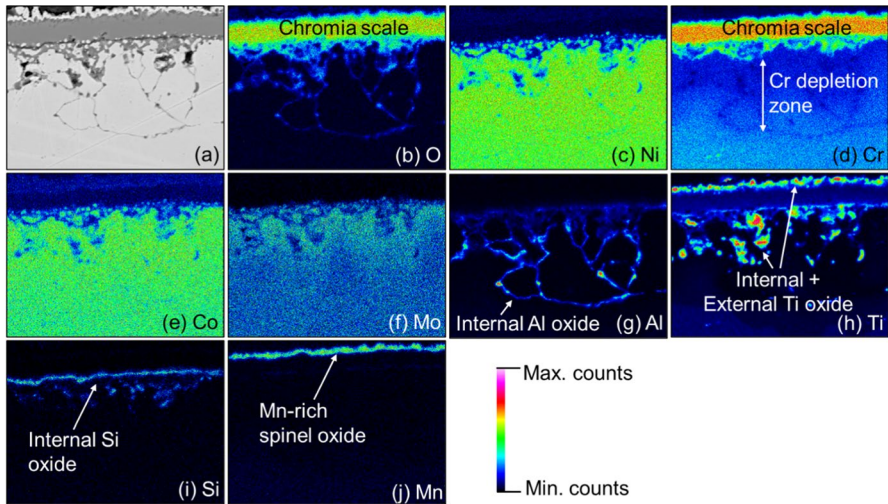

Fig. 3 Cross-sectional analysis of Alloy 263 exposed to 1 bar of 95% $CO_2 + 4\%$ $H_2O + 1\%$ O_2 at 750 °C for 2500 h. **a** SEM reference image, **b–j** Qualitative EPMA X-ray maps showing elements of interest

The alloys are arranged from top to bottom in Fig. 2 in the order of thinnest to thickest chromia scale formed at temperature of 750 °C. In a previous study we showed that the chromia scale thickness at these conditions tended to increase with Ti content and decrease with Si and Mn contents [6]. According to the scale thicknesses observed in Fig. 2, the same trend appears to hold true at temperatures of 700 and 800 °C, the main exception being alloy 230 at 800 °C, which formed among the thickest chromia scales of all the alloys (Fig. 2k). EDS mapping of the scale formed on alloy 230 at 800 °C (data not shown) confirmed it was indeed chromia, with no evidence of Ni-rich oxides. In addition to an external chromia scale, some other features are evident from Figs. 2 and 3, such as the formation of interfacial and subsurface voids that are gradually filled during the oxidation process. The details of these void formation/filling processes were described previously for a Ni-based alloy exposed to pure CO_2 at 700 °C [25, 26]. The similar appearance of features in Figs. 2 and 3, combined with the observation that these features were essentially identical for alloys exposed to $CO_2 + 4\%H_2O + 1\%O_2$ as those exposed to pure CO_2 [17], suggests that these processes are also operative for the conditions tested herein. While not shown in Fig. 2, the reproducibly low mass gains for all alloys exposed without SO_2 at 600 and 650 °C (Fig. 1) suggest that thin chromia scales likewise formed at these temperatures. In short, in the absence of SO_2, all tested alloys formed thin protective chromia scales at temperatures ranging from 600 to 800 °C.

Characterization of Sulfur Effects at 600 °C

According to Fig. 1, the alloy which showed the strongest influence of SO_2 at 600 °C was alloy 617. Figure 4 presents various characterization results for this alloy. Figure 4a, b compare the oxide scale formed without and with SO_2, respectively, indicating that indeed SO_2 caused a substantial increase in the thickness of the scale (Fig. 4b). Quantitative X-ray maps of the SO_2-exposed sample reveal a duplex oxide scale, where the outer layer contains primarily Ni and the inner layer contains all of the base metals and is slightly enriched in Cr. Meanwhile, S is present throughout the inner layer and near the outermost surface of the scale. The S present at the outermost surface is correlated with Ni and Co. X-ray diffraction (XRD) results (Fig. 4c) confirm that Cr_2O_3 (chromia) was the primary reaction product in the absence of SO_2, while MoNi intermetallic phase is also detected. These are the bright contrast particles observed immediately below the chromia scale (Fig. 4a) and likely formed during oxidation in a way that is analogous to what been observed previously for Ni_3Nb particles formed beneath chromia scales grown on alloy 625 [27]. Alternatively, XRD of the SO_2-exposed sample reveals NiO and Ni-rich sulfate as the primary reaction products. It is noteworthy that the sulfates of Ni and Co (MSO_4 where M = metal) exhibit similar structure that is difficult to differentiate in the XRD spectra. Further, considering the information depth of the XRD measurement (on the order of 10 μm), it is reasonable to assume that sulfate compounds identified by XRD correspond to the S-rich regions near the outermost portion of the scale (Fig. 4e). Hence, the reaction product formed on alloy 617 in the SO_2-containing exposure at 600 °C consists of a non-protective duplex oxide scale and an outermost
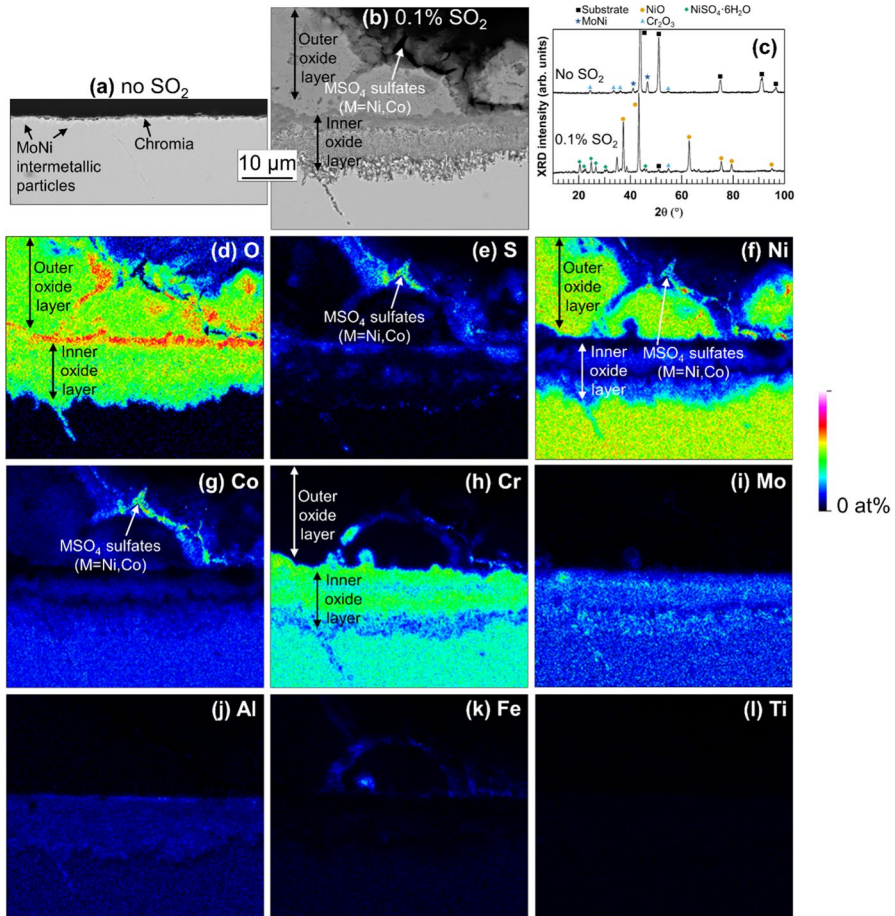
Fig. 4 Analysis of Alloy 617 exposed to 1 bar of 95% CO_2 + 4% H_2O + 1% O_2 with and without 0.1% SO_2 at 600 °C for 2500 h. **a**, **b** Cross-sectional SEM images of samples exposed with and without SO_2, **c** XRD of samples exposed with and without SO_2, **d**–**l** Quantitative EPMA X-ray maps of the region shown in (**b**)

layer of Ni- and Co-rich sulfates. Additional minor peaks are also present for the SO_2-exposed sample in Fig. 4c which we were unable to index, suggesting perhaps the presence of small amounts of additional complex oxides.

Characterization of Sulfur Effects at 700 °C

The other temperature which showed significant effects of SO_2 was 700 °C, and cross-sectional SEM images of several of the alloys exposed at this temperature are shown in Fig. 5. As shown in Fig. 2 previously, all alloys exposed without SO_2 (Fig. 5a–e) formed a thin chromia scale at 700 °C, with occasional small
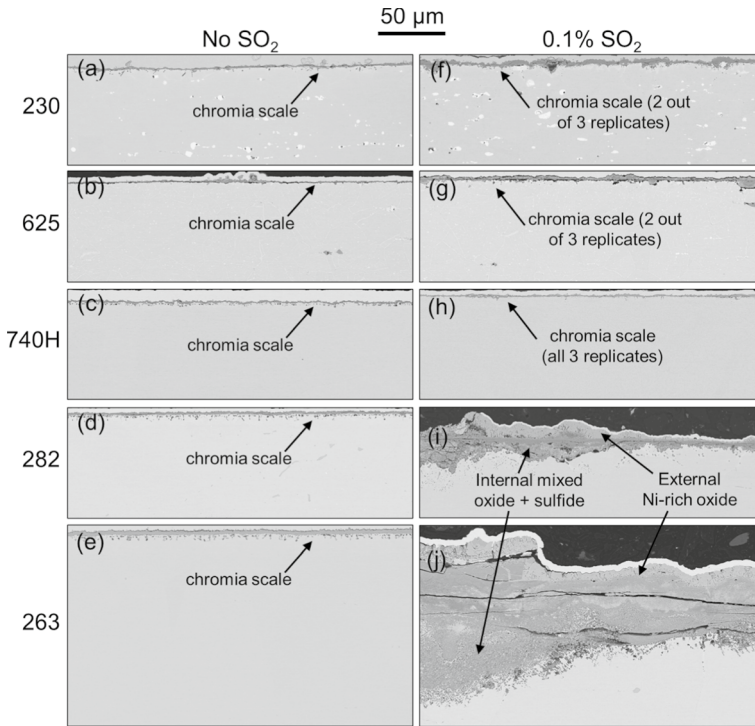
Fig. 5 Cross-sectional SEM images of various Ni-based alloys exposed at 700 °C for 2500 h to **a–e** 1 bar of 95% CO_2 + 4% H_2O + 1% O_2, **f–j** the same gas containing 0.1% SO_2

oxide nodules such as those seen in Fig. 5a, b. The presence of a chromia scale in the absence of SO_2, albeit clear from the appearance of the scales in Fig. 5 and the corresponding low mass gains (Fig. 1e), was further confirmed via X-ray mapping for several of the alloys (data not shown). The only alloy to also form a thin and uniform chromia scale in the presence of SO_2 for all three replicate samples tested was alloy 740H, as shown in Fig. 5h and reflected by the low mass gains and small error bars in Fig. 1f. In addition, two out of the three replicate samples of both alloys 230 and 625 (including those shown in Fig. 5) exhibited mass gains only slightly higher than the SO_2-free case, consistent with the slightly thicker chromia scales in Fig. 5f, g. Alternatively, one replicate sample of both these alloys showed notable mass losses at times ≥ 1000 h. For both alloys 282 and 263, one replicate sample of each alloy showed low mass gains characteristic of chromia scales, while the other two replicates showed significant mass gains and/or losses, as reflected by the large error bars in Fig. 1f. Figure 5i, j shows results from these more corroded replicates, confirming that a much thicker scale was formed on these samples compared to the SO_2-free condition.
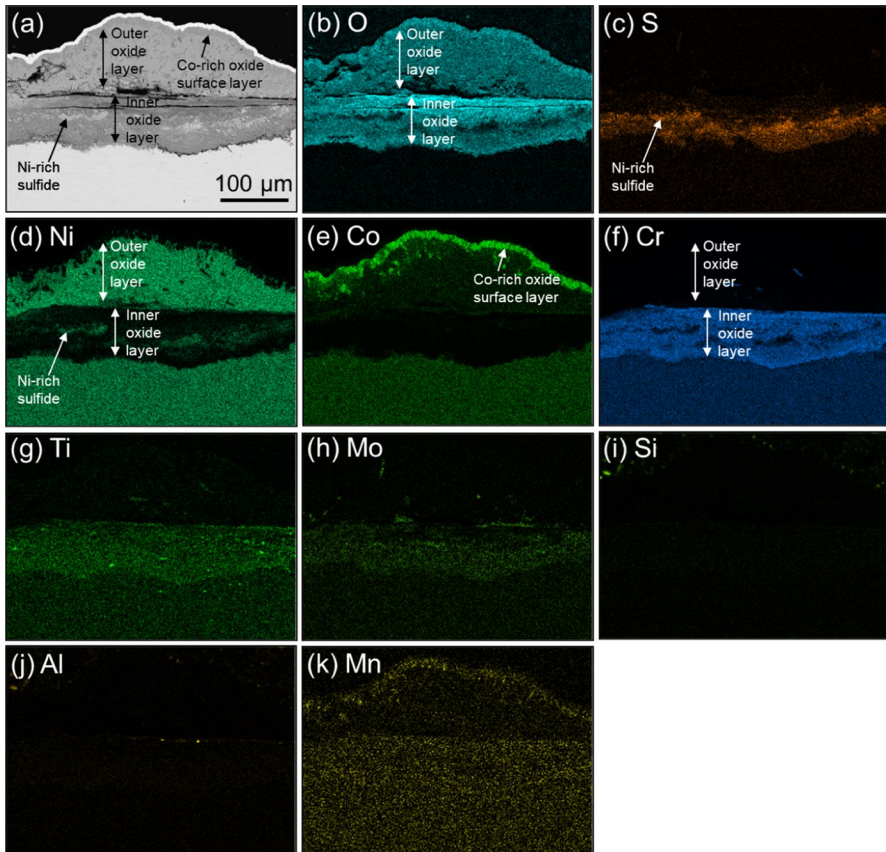
Fig. 6 Cross-sectional analysis of Alloy 263 exposed to 1 bar of 95% CO_2 + 4% H_2O + 1% O_2 + 0.1% SO_2 at 700 °C for 2500 h. **a** SEM image of the whole oxide scale. **b–k** EDS X-ray maps showing elements of interest

Figure 6 shows a relatively low-magnification cross-sectional SEM image and corresponding EDS X-ray maps for alloy 263 exposed to the SO_2-containing gas at 700 °C. Similar to alloy 617 exposed at 600 °C (Fig. 4), the scale consists of a non-protective duplex oxide, where the outer layer contains primarily Ni and the inner layer contains all the base metals and is enriched in Cr, while sulfur is distributed throughout the inner layer. However, unlike alloy 617 at 600 °C, no sulfur was evident near the external surface of the scale for alloy 263 exposed at 700 °C, which instead consisted of an outermost layer of Co-rich oxide.

Figure 7 shows higher magnification SEM and EDS analysis near the scale/alloy interface. Cr-rich sulfides are observed near the grain boundaries ahead of the inward-growing oxidation front, accompanied by significant Cr depletion adjacent to the boundaries to the depths where these sulfides have formed. Some enrichment of Co is observed where Cr is depleted; however, close inspection of Fig. 7f suggests the enrichment of Co is more generalized and does not correlate precisely
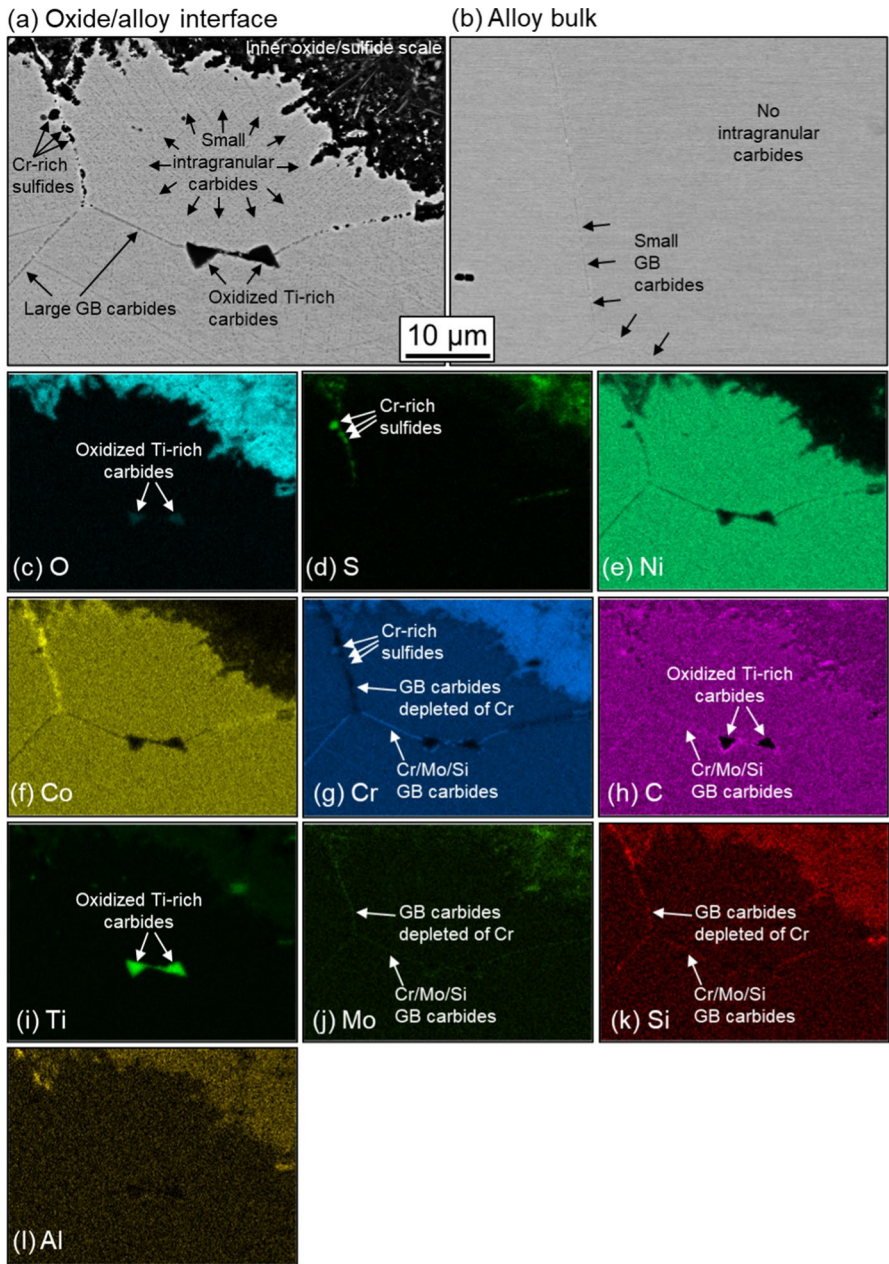
Fig. 7 Cross-sectional analysis of Alloy 263 exposed to 1 bar of 95% CO_2 + 4% H_2O + 1% O_2 + 0.1% SO_2 at 700 °C for 2500 h. **a** SEM image of the inward-growing oxidation front. **b** SEM image of the alloy bulk far from the oxidation front, collected using identical imaging conditions. **c–l** EDS X-ray maps showing elements of interest for the region shown in (**a**). GB = grain boundary

with S (Fig. 7d) compared to the case of Cr (Fig. 7g). Hence, the Co enrichment is likely primarily a consequence of Cr depletion in these regions, and not Co-rich sulfides. Meanwhile, relatively large carbides are observed along the grain boundaries. Notably, the grain boundary carbides contain Cr (Fig. 7g), Si (Fig. 7k), and Mo (Fig. 7j) at depths beneath which the Cr-rich sulfides formed, whereas only Si and Mo are detected at the grain boundary at the shallower depths where Cr-rich sulfides are observed. Comparison to a region far from the oxidation front (Fig. 7b) indicates that the grain boundary carbides are much more prominent immediately below the oxide scale, compared to the alloy bulk. Further, small intragranular carbides are observed in the regions beneath the oxide scale (Fig. 7a) that were not present in the alloy bulk (Fig. 7b). Close inspection of Fig. 7a, g indicates that these intragranular carbides are enriched in Cr and appeared to form preferentially at subgrain boundaries in the alloy. Hence, it is deduced that carburization of the alloy accompanied growth of the non-protective duplex oxide scale during exposure to the SO_2-containing gas. Finally, triangular-shaped Ti-rich oxides are observed at the grain boundaries (Fig. 7c, i), while some carbon enrichment is seen adjacent to them (Fig. 7h). Particles of similar shape and size that were observed in the bulk of the alloy (not shown) were found to be Ti-rich carbides. Hence, the Ti-rich carbides present at the grain boundary slightly ahead of the inward-growing oxidation front were partially oxidized during the exposure.

Figure 8 shows similar cross-sectional SEM and EDS analysis of alloy 282 exposed to the SO_2-containing gas at 700 °C. Unlike alloy 263, which showed rather uniform and extensive corrosion across the sample, alloy 282 contained some regions of similarly extensive attack and other regions where the attack was much less severe (i.e., stunted attack), as shown in Fig. 8a. Figure 8b–j shows higher-magnification SEM and EDS analysis of the region indicated in Fig. 8a, i.e., near the scale/alloy interface of a region that experienced less severe attack. Many relatively larger Cr-rich sulfides and relatively smaller Ti-rich sulfides are seen to depths of ≈20–30 μm beneath the scale.

Characterization of Sulfur Effects at 800 °C

Figure 9 shows cross-sectional SEM images of several of the alloys exposed with and without SO_2 at 800 °C. While not as drastic as the exposures done at lower temperatures, some notable differences are observed. In particular, the extent of internal oxidation was more severe in the presence of SO_2. As with 700 °C results, alloy 263 was the most affected by the presence of SO_2, albeit to a much lesser extent compared to 700 °C. While the SO_2-free sample showed a rather uniform chromia scale and limited evidence of spallation, the SO_2-containing sample instead consisted of an outer Ni-rich oxide layer and an inner non-uniform layer of Cr-rich oxide that had grown several μm into the alloy substrate. In addition, Cr-rich sulfides were observed beneath the scale formed on alloy 263 at 800 °C, whereas they were rarely observed beneath the scales formed on the other alloys at this temperature.
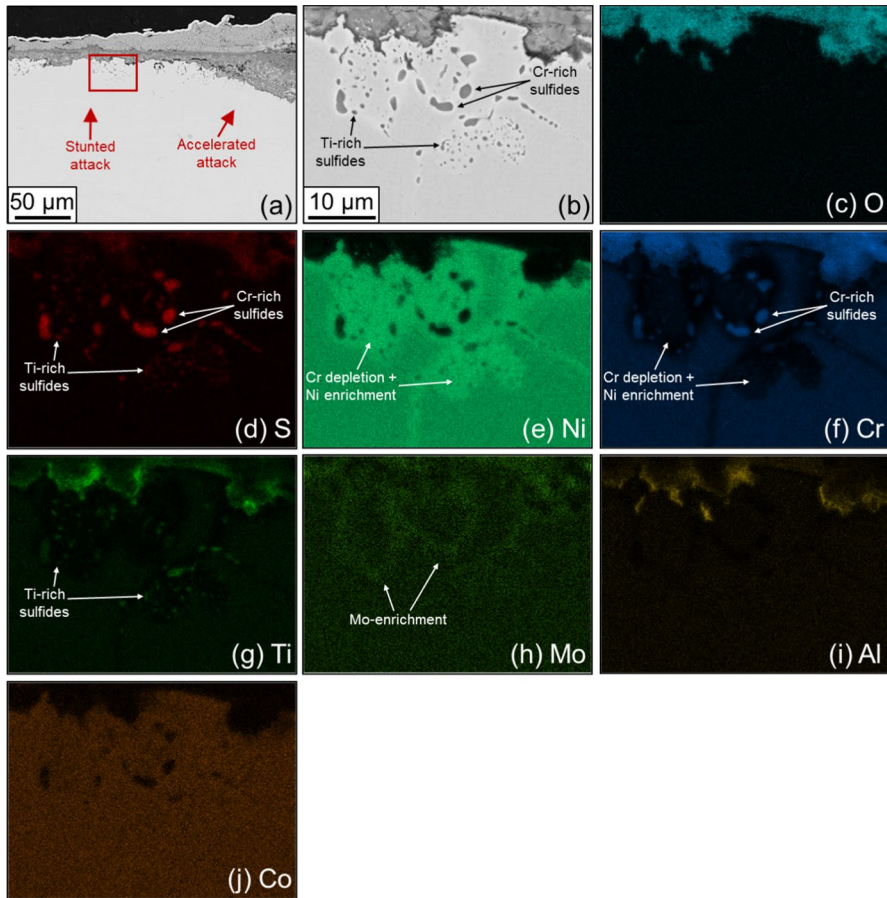
Fig. 8 Cross-sectional analysis of Alloy 282 exposed to 1 bar of 95% CO_2 + 4% H_2O + 1% O_2 + 0.1% SO_2 at 700 °C for 2500 h. **a** Low-magnification SEM image. **b** High-magnification SEM image of the red box in part **a**, as an example of the inward-growing oxidation front at a region of stunted attack. **c**–**j** EDS X-ray maps of the region shown in part (**b**)

Oxidation Rate Constants

A convenient way to visualize and compare this rather large set of alloy oxidation data is by calculating a reaction rate constant for each alloy and condition. A simplified version of the parabolic oxidation rate constant, k_p, which considers only the mass change at the conclusion of the 2500 h exposure, may be calculated according to

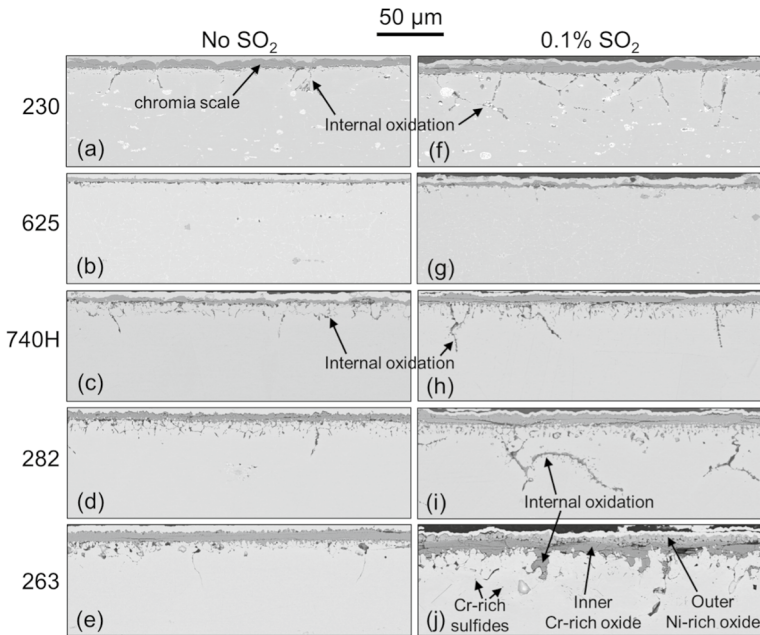$$k_{\mathrm{p}} = \frac{(\Delta m)^2}{2t} \tag{1}$$

Fig. 9 Cross-sectional SEM images of various Ni-based alloys exposed at 800 °C for 2500 h to **a–e** 1 bar of 95% CO_2 + 4% H_2O + 1% O_2. **f–j** the same gas containing 0.1% SO_2

where Δm is the mass change per unit area and t the exposure time. When the mechanism of oxidation is unchanged over a given temperature range, the temperature dependence can then be described by an Arrhenius relationship according to

$$k_p = k_{p,o}\left(e^{-\frac{E_a}{RT}}\right) \tag{2}$$

where $k_{p,o}$ is the pre-exponential constant, E_a the activation energy, R the gas constant, and T the absolute temperature. Strictly speaking, it is not appropriate to calculate parabolic oxidation rate constants from mass change data when significant spallation, resulting in overall mass losses, has occurred (e.g., several alloys exposed in the presence of SO_2 at 700 °C). As such, rate constants for the SO_2-containing exposures do not reflect actual oxide growth rates and hence should not be used for oxidation lifetime modeling, for example. Nevertheless, the rate constants still capture the magnitude of degradation since large mass losses correspond to large k_p values in the simplified expression for k_p defined in Eq. 1 (i.e., k_p being proportional to the square of the mass change and thus always being a positive value). Thus, the k_p values according to Eq. 1 are presented in Fig. 10.

Figure 10a indicates that in the absence of SO_2, all alloys exhibited low rate constants that are generally consistent with the values expected for chromia scale growth [28, 29]. Note that the very small mass gains for exposures done without SO_2 at 600 and 650 °C approached the limit of the microbalance for many of the alloys. The alloys which showed relatively larger mass gains at 600–650 °C, (263
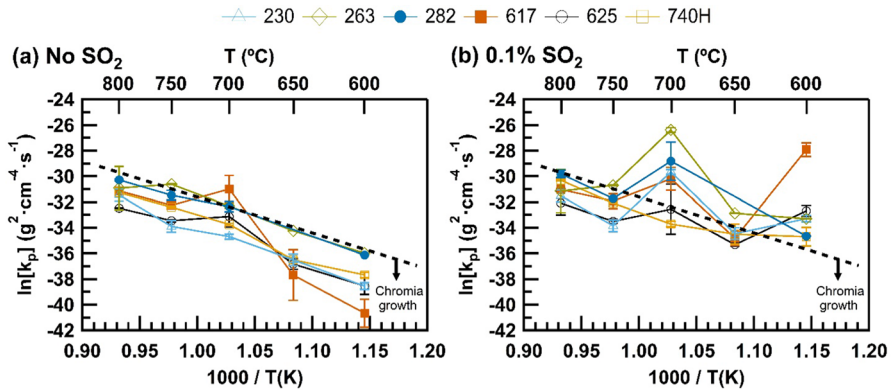
Fig. 10 Parabolic oxidation rate constants of Ni-based alloys exposed to 1 bar of **a** 95% CO_2 + 4% H_2O + 1% O_2, **b** the same gas containing 0.1% SO_2, at temperatures of 600–800 °C

and 282) and all alloys at temperatures ≥ 700 °C, showed a clear Arrhenius-type temperature dependence. That is, the results exhibit a linear relationship between the $\ln[k_p]$ and inverse of temperature, according to Eq. 2. The primary exception was alloy 617 exposed at 700 °C, which showed a higher-than-expected rate constant. Table 2 summarizes the Arrhenius fitting results and associated R-squared values for the alloys exposed without SO_2. Except for 617, the alloys exhibited activation energies ranging from 220 to 260 kJ/mol, in general agreement with values expected for the growth of chromia scales [28, 29].

Compared to the SO_2-free exposures, the alloys exposed with SO_2 showed a temperature dependence that was much more complex. The alloys largely exhibited rate constants that were similar or only slightly higher than those expected for chromia scale growth at temperatures of 650, 750, and 800 °C, consistent with the characterization results shown previously. Alternatively, the rate constants were slightly or significantly higher than those corresponding to chromia scale growth at temperatures of 600 and 700 °C, again consistent with the characterization results presented earlier.

## Thermodynamic Considerations of Sulfur Effects

To begin to understand the pattern of oxidation behavior in the SO_2-containing exposures, it is prudent to consider the thermodynamic aspects which can affect

Table 2 Results of the Arrhenius fitting (Eq. 2) of parabolic oxidation rate constants of Ni-based alloys exposed to 1 bar of 95% CO_2 + 4% H_2O + 1% O_2 (Fig. 10a)

	230	263	282	617	625	740H
$k_{p,0}$ (g^2 cm^{-4} s^{-1})	0.079	0.0029	0.0094	1.1×10^6	0.012	0.22
E_a (kJ mol^{-1})	260	220	230	390	250	260
R^2	0.98	0.94	0.99	0.82	0.88	0.98

sulfur-induced corrosion in these environments [19–22, 30]. Figure 11a plots the equilibrium partial pressures (activities) of SO_2, SO_3, and S_2 at each temperature. Notably, the ratio of the two major sulfur-containing gas species, SO_3/SO_2, is roughly unity at 600 °C and decreases with temperature. Alternatively, the sulfur activity of the gas (i.e., pS_2), which may be thought of as the general driving force for sulfidation, increases by approximately nine orders of magnitude over the temperature range. To determine the compounds expected to be stable in contact with this gas, and importantly the effect of temperature on the relative stability of these compounds, thermochemical diagrams of the M–O–S system were generated for metals present at high concentrations in the alloys (i.e., Ni, Cr, and Co). Figure 11b shows an example for pure nickel at two temperatures, 550 °C (blue dashed lines) and 750 °C (orange solid lines). Within this three-component

Fig. 11 Thermodynamic analysis relevant to exposures done in the SO_2-containing gas. a Equilibrium partial pressures of SO_2, SO_3, S_2 at each temperature. b Thermochemical diagram showing the metal, oxide, sulfide, and sulfate phase fields for pure Ni as a function of pO_2 and pSO_2 of the equilibrium gas at temperatures of 550 °C (blue dashed lines) and 750 °C (orange solid lines). c Showing the oxide/sulfate phase boundary for pure Ni, Co, and Cr as a function of temperature and pSO_2 compared to the pSO_2 of the equilibrium gas (Color figure online)
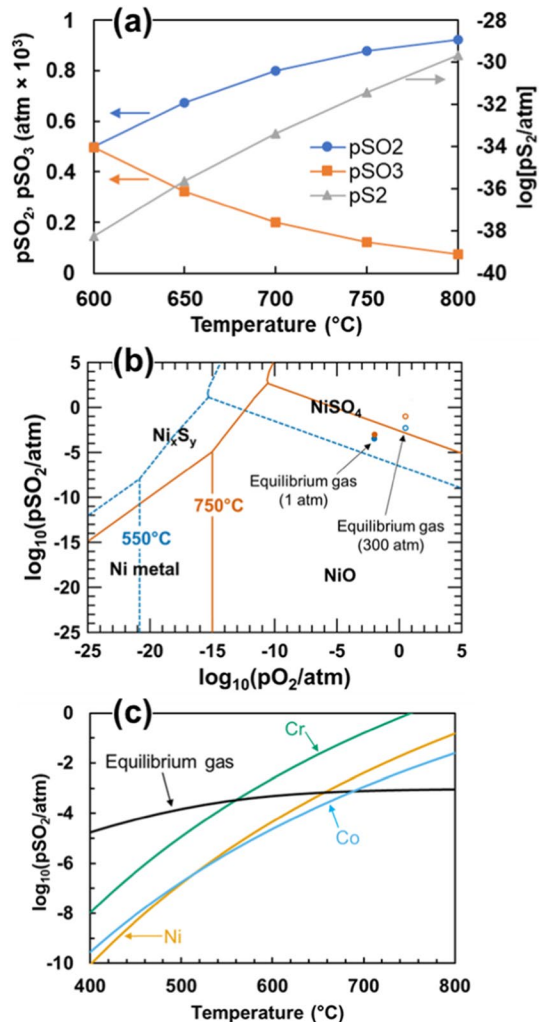
system, the gas can be uniquely defined by two species. For convenience, these are selected as pSO_2 and pO_2. Four different phase regions are observed, namely pure Ni (low pO_2 and low pSO_2), nickel sulfide (low pO_2 and high pSO_2), nickel oxide (high pO_2 and low pSO_2), and nickel sulfate (high pO_2 and high pSO_2). Note that for clarity, only the phase boundaries for the most nickel-rich of the sulfides is shown. The equilibrium gas composition at 1 atm (1 bar) total pressure for both these temperatures are superimposed on the diagram. This analysis shows that at a temperature of 750 °C, the oxide is the stable phase of nickel in contact with the gas. Alternatively, at a temperature of 550 °C, although the equilibrium gas composition has not changed significantly, the phase boundary between the oxide and sulfate of nickel has shifted to significantly lower pO_2 and pSO_2. The shift is so significant that the equilibrium gas composition now lies firmly within the nickel sulfate phase field. The above analysis illustrates that there is a critical temperature, above which the oxide is the stable form of Ni in contact with the gas, and below which sulfate is the stable form. This concept is illustrated in Fig. 11c, where the pSO_2 of the equilibrium gas is compared to the pSO_2 corresponding to the oxide/sulfate phase boundary (i.e., activity of the oxide = activity of the sulfate = 1). The point of intersection is the temperature below which the stable form of the metal changes from oxide to sulfate. This analysis shows that the transition temperature for the most important (pure) metals relevant to the alloys tested herein are 561 °C (Cr), 657 °C (Ni), and 688 °C (Co).

Discussion

General Remarks

The following points summarize the key results presented above:

- With very few exceptions, all alloys formed protective chromia scales throughout the entire 2500 h exposure when tested in 95% CO_2, 4% H_2O, 1% O_2 at temperatures of 600–800 °C.
- The addition of 0.1% SO_2 caused virtually no differences in oxidation behavior at 750 °C, caused only minor differences at 650 and 800 °C, but significantly increased the extent of oxidation for several of the alloys at temperatures of 600 and 700 °C.
- At 600 °C, the scale of the most significantly attacked alloy (i.e., alloy 617) consisted of a non-protective duplex oxide and an outermost layer of Ni/Co-rich sulfate.
- At 700 °C, the scale of highly attacked alloys (e.g., alloy 263) was similar to the above, except that no sulfates were observed.
- Thermodynamic analyses indicated that a transition in stable compound of the main metals comprising the alloy from oxide to sulfate is predicted with decreasing temperatures in the range of approximately 700–550 °C.

First, it should be noted that, in the absence of SO_2, currently available Ni-based alloys do not appear to be susceptible to increased oxidation rates in high-temperature CO_2 caused by relatively high levels of water and oxygen impurities, such as those expected in direct-fired supercritical CO_2 power cycles, within the temperature range ($\approx$600–800 °C) at which they are envisioned to operate. Nevertheless, at higher pressures and flow velocities present in real sCO_2 systems, additional degradation modes such as water vapor-assisted chromia volatilization may become important [16].

Regarding exposures done in SO_2, it is well known that sulfur, whether in the gas phase or as a deposit on the alloy surface, can significantly increase the corrosion rate of Ni–Cr based alloys [30]. The question of interest is essentially whether the alloy can form and maintain a protective chromia scale at the given conditions. In highly sulfidizing environments (i.e., equilibrium close to the oxide/sulfide phase boundary), a common occurrence is that sulfides and oxides form simultaneously, which not only prevent the formation of a protective chromia scale but also create continuous networks of sulfide compounds throughout the scale [19]. These sulfides can both accelerate cation diffusion, resulting in very high oxidation rates, or simply melt at temperatures above $\approx$645 °C (the Ni-S eutectic temperature) and destroy any protectiveness of the oxide. It is noteworthy that the alloys which suffered increased attack in the SO_2-containing gas (e.g., 617 at 600 °C and 263 at 700 °C) did not show appreciable quantities of sulfur in the outward growing, Ni-rich oxide portions of the scale (Figs. 4 and 6). Furthermore, the oxide scale thicknesses observed for those alloys are within the range expected for growth of NiO on pure Ni at these temperatures [31]. Hence, we deduce that the role of sulfur was essentially to disrupt the formation and/or growth of a chromia scale, resulting in faster-growing nonprotective oxide scales rich in the base metal. We now consider how this process occurred, focusing first on the temperatures at which sulfate formation was not possible, i.e., $T \geq 700$ °C.

Impact of SO_2 at 700–800 °C

At 700 °C, the mass gains suggest that an incubation period preceded the accelerated attack. That is, all the alloys showed small mass gains (< 0.4 mg/cm^2), similar to the SO_2-free case, after the first 500 h of exposure (Fig. 1f). This scenario is similar to the one encountered when an alloy is pre-oxidized, then subsequently exposed to a sulfur-containing environment [21]. In these cases, the pre-formed oxide layer (usually chromia) delays the accelerated attack, but often not indefinitely. Under these circumstances, it has been shown that, despite the presence of a protective chromia scale, sulfur in some form remains able to diffuse through the oxide (probably via grain boundaries [32]), where it then tends to preferentially react with Cr in the underlying alloy to form Cr-rich sulfides. This is possible even for environments, such as ours, where sulfide formation in contact with the gas cannot occur (Fig. 11). This is explained by the locally elevated sulfur activities beneath the oxide, where oxygen activities are very low [33, 34]. It has been suggested that eventually this process results in a 'critical microstructure' whereby the above-growing chromia

scale fails, and accelerated attack ensues [35]. This process appears to effectively explain the increased attack observed at 700 °C. For example, the analysis shown in Fig. 8b–j captures a region of alloy 282 where the accelerated attack was interrupted due to the formation of a Cr-rich oxide layer at the inward-growing oxidation front. Significant sulfide formation is observed in this region, and it is likely that with continued exposure, the region would eventually succumb to accelerated attack, similar to that seen near the right side of Fig. 8a. When the alloy is currently undergoing accelerated attack, significant sulfide formation does not accumulate in the alloy due to the fast inward-growth of the oxide, but nevertheless subsurface sulfide formation continues to occur, apparently preferentially along the grain boundaries (Fig. 7), inhibiting recovery in the form of a new Cr-rich oxide layer at the oxide/alloy interface. The 'critical microstructure' interpretation [35] typically emphasizes the role of Cr sulfide formation and its subsequent oxidation (as the sulfides are incorporated into the inward-growing oxide layer) as the reason for eventual failure, but another possibility in this case involves the formation of liquid metal sulfides. That is, as Cr becomes severely depleted in these regions, eventually Ni sulfide formation may occur. Nickel sulfide exhibits a eutectic point at approximately 645 °C [30], and hence, above this temperature melting can occur. Some evidence of this is seen for alloy 263 in Fig. 6, where regions of nickel sulfide bands are observed parallel to the oxidation front at various depths of the inward-growing, inner oxide layer. This hints at the possibility that nickel sulfide formed at the (then) alloy/oxide interface after sufficient Cr depletion had occurred, possibly melting and thereby triggering accelerated attack in those regions. Finally, it is noteworthy that once the alloy enters into the accelerated corrosion regime (i.e., growth of the non-protective duplex oxide scale), this is accompanied by significant carburization of the alloy (Fig. 7). The carburization manifests as carbides enriched in Cr at both the grain boundaries and grain interiors. This process depletes metallic Cr from the alloy matrix, effectively reducing the flux of Cr toward the surface to support formation of a continuous Cr-rich oxide scale. Notably, the depth of carburization into the alloy is much deeper than the depth of sulfide formation (Fig. 7). Hence, it is reasonable to speculate that, once the chromia scale fails and non-protective oxide growth begins, recovery from this accelerated corrosion process is made more difficult by the fact that the alloy is then highly susceptibility to carburization.

To summarize, at 700 °C the increased extent of oxidation for several of the alloys in the SO_2-containing environment reflects that the chromia scales initially formed on these alloys were not perfect barriers to sulfur ingress, which eventually resulted in their failure and subsequent growth of non-protective duplex oxide scales. The question is then why were certain alloys more susceptible than others? The most obvious explanation is that the most susceptible alloys, namely 263 and 282, contained the lowest Cr content among the alloys tested (Table 2), making it generally more difficult to establish and maintain a chromia scale. Still, the most attacked alloy, 263, contained more Cr (19.9 wt%) compared to the relatively lesser attacked alloy 282 (19.2 wt%). Also worth noting is that these two alloys tended to form the fastest growing (thickest) chromia scales in the absence of SO_2 (note that the alloys are arranged in order of increasing chromia scale thickness in Fig. 5a–e), and indeed the fastest growing chromia scale belonged to the most susceptible alloy,

i.e., 263. Hence, the combination of a faster-growing chromia scale, and a relatively low Cr content of the alloy to begin with, resulted in the most severe Cr depletion conditions and thereby the greatest susceptibility to accelerated corrosion following the process described above. The only alloy where the oxidation behavior at 700 °C did not appear to change at all with the addition of SO_2 was alloy 740H, which contained the highest Cr content (24.5 wt%) among the alloys tested. This provides further support to the notion that the accelerated attack was largely a question of the extent of Cr depletion in the alloy. It is worth mentioning that many of the alloys tested herein do carburize, albeit at very small rates, during growth of protective chromia scales in high-temperature CO_2 [4]. Notably, alloy 263 is among the most resistant to carburization during chromia scale growth, owing to its relatively high Si and Mn contents [4]. Hence, it is unlikely that alloy carburization during growth of the chromia scale played a role in the eventual failure of this scale. Carburization during subsequent growth of the non-protective duplex oxide scale may, however, perpetuate the accelerated corrosion, as described above.

At a higher temperature of 750 °C, no evidence of any effect of SO_2 could be found, as described in detail in a prior study [6] and reflected by the very similar mass gains with/without SO_2 (Fig. 1g, h). At still higher temperature of 800 °C, some evidence of the beginnings of accelerated attack in SO_2 becomes apparent once again, particularly for alloy 263. This complex temperature dependence of the effect of SO_2 at temperatures of 700–800 °C is challenging to explain. Nevertheless, the following five points are likely relevant. As the temperature increases:

1. The pS_2 of the gas, and thus the thermodynamic driving force for sulfidation, increases.
2. The chromia scales grew at a faster rate, increasing their susceptibility to cracking during thermal cycling, which could create pathways for increased sulfur ingress.
3. The amount of SO_3 in the gas (which may be the problematic molecule diffusing through the oxide and supplying sulfur to the alloy) decreases.
4. Diffusion in the alloy increases, potentially making the alloy less susceptible to significant Cr depletion associated with internal sulfide formation.
5. The tendency for strongly adsorbing sulfur-containing molecules to preferentially occupy surface sites on (and within) the oxide, and therefore gain access to the underlying alloy, decreases. That is to say, the tendency for preferential adsorption of sulfur molecules decreases with increasing temperature [36, 37].

Of the above five points, the first two would tend to increase, and the last three decrease, the susceptibility of the alloy to accelerated attack caused by SO_2 impurities, as the temperature increases. The convolution of these (and possibly additional) factors gives rise to the complex temperature dependence observed in the temperature range of 700–800 °C.

Impact of SO$_2$ at 600–650 °C

We now turn to temperatures ≤ 650 °C, where sulfate formation of various metals in the alloy becomes possible. SO$_2$ additions caused slightly higher mass gains for all the alloys at 650 °C, although the oxidation rates were still close to those expected for chromia scale growth (Fig. 10). At 600 °C, the effect was more pronounced, now placing many of the alloys at oxidation rates firmly above those expected for chromia growth (Fig. 10). Characterization of the most extensively attacked alloy 617 showed many of the same corrosion features as those of the susceptible alloys exposed at 700 °C, i.e., outer Ni-rich oxide layer, inner mixed oxide layer enriched with Cr, and sulfides dispersed throughout (and below) the inner oxide layer. The key difference of course is that sulfates of Ni and Co were also observed at the oxide scale surface. An important question then is whether sulfate formation is the cause, or consequence, of the accelerated attack at this temperature. As described above, the sulfates of pure Ni and Co become stable at temperatures below 657 °C and 688 °C, respectively, whereas the oxide remains the stable form of Cr (transition temperature 561 °C). Therefore, it is reasonable to speculate that the alloy simply failed to form a chromia scale, in a manner analogous to the one described above for 700 °C exposures. Then, the resulting external oxide layer rich in Ni and Co provided an activity of these metals at the surface of the oxide that was sufficient to form their sulfate compounds. Alas, this explanation is not satisfying for two reasons. First, at the higher temperatures, alloy 263 and to a lesser extent alloy 282, were the most severely attacked, and the reasons for this were convincing (lower Cr contents and faster-growing chromia scales). There is no obvious reason why this would be presumed different at lower temperatures, yet these alloys were much less attacked compared 617. Second, while accelerated attack at 700 °C always followed an incubation period (note the small mass gains for all alloys after 500 h in Fig. 1f), accelerated attack of 617 at 600 °C was already apparent after the first 500 h exposure iteration (Fig. 1b). These observations suggest a different mechanism may be at play at 600 °C. Specifically, it hints at the possibility that formation of the sulfates of Ni and Co during the transient stages of oxidation prevented the establishment of a chromia scale. Assuming this to be the case, the reason it did not occur at 650 °C (which is also below the oxide/sulfate transition temperature of Ni and Co), may be related to the so-called kinetic boundary [30, 38], whereby the chemical activities necessary to promote a phase transition are higher than predicted thermodynamically. This is typically discussed in the context of the sulfide-to-oxide phase transition, although the same logic applies here for the oxide-to-sulfate transition. In addition, the thermodynamic predictions in Fig. 11 are based on pure metals, whereas the activities of Ni and Co will be different (lower) in the real materials, likewise affecting the transition temperature. From an application perspective, it is also noteworthy that the analysis described herein considers atmospheric pressure gases, whereas real sCO$_2$ power systems will operate at much higher pressures. This can further push reaction product stability toward the sulfate phase field, as indicated by the hollow circles in Fig. 11b, considering a pressure of 300 atm as an example.

Regardless of the precise mechanism of accelerated attack at 600 °C, the reason that alloy 617 was uniquely susceptible is puzzling. It is noteworthy that alloy 617

was similarly attacked during exposure to another CO_2-rich environment containing small amounts of SO_2 at a temperature of 550 °C [8]; hence, the effect appears reproducible. There is no obvious explanation by comparing alloy compositions, considering that 617 contained a higher level of Cr and lower level of Co (and lower level of Ni+Co) compared to alloy 263, for example (Table 1). While admittedly quite speculative, one possibility relates to the role of minor alloying elements. Alloy 617 contains the least Si among the alloys tested and relatively lower Ti than the alloys that may otherwise be expected to be susceptible based on the higher temperature results (i.e., alloys 263 and 282). Because Si and Ti form very stable oxides and diffuse quickly in the alloy, their segregation to the surface of the oxide during the transient stages would be expected. Because they do not form stable sulfate compounds, the presence of these minor additions at sufficient concentration in the alloy may reduce the activity of the sulfate-forming elements (e.g., Ni) at the surface of the oxide to a level sufficient to suppress sulfate formation, allowing time for the establishment of a protective chromia scale.

Summary and Conclusions

The high-temperature corrosion behavior of several commercial Ni-based alloys was evaluated in atmospheric pressure gases intended to simulate the compositions expected in direct-fired supercritical CO_2 power cycles. The presence of 4% H_2O and 1% O_2 in the CO_2 gas produced no evidence of accelerated corrosion, where all alloys formed and maintained protective chromia scales with growth rates that followed an Arrhenius dependence across the temperature range of 600–800 °C. Further additions of 0.1% SO_2 did, however, accelerate the corrosion of several of the alloys across the same temperature range. At relatively high temperatures (700 °C), accelerated corrosion was caused by ingress of sulfur through an initially protective scale, leading to formation of internal Cr-rich sulfides and severe Cr depletion in the underlying alloy. This caused eventual scale failure, resulting in formation of a non-protective duplex oxide scale. Growth of this non-protective scale was accompanied by severe carburization of the alloy, which may have further contributed to the inability of the alloy to recover from the accelerated corrosion process induced by sulfur. Alloy susceptibility to the above process was strongly correlated with Cr content, with alloys containing less than approximately 20 wt% showing high susceptibility. At relatively lower temperature (600 °C), no such correlation was observed between accelerated corrosion caused by SO_2 additions and Cr content of the alloy. At these lower temperatures it is suggested that the accelerated corrosion was driven by the formation of metal sulfates during the early stages of oxidation, preventing the establishment of a protective chromia layer and again resulting in growth of a non-protective duplex oxide scale.

The results suggest that, in the absence of sulfur impurities, rapid oxidation of Ni-based alloys is not likely to be a concern in future direct-fired sCO₂ systems; however, additional degradation modes such as water–vapor-assisted oxide volatilization remain potentially problematic, as reported previously. Alternatively, if sulfur-based impurities are expected, the selection of Ni-based alloys requires careful

consideration. Accelerated attack is clearly possible in this case and the mechanisms responsible appear to be multifaceted, resulting in a complex dependence on both exposure temperature and alloy composition. Notably, 740H was the only alloy to perform well across the whole temperature regime for all replicate samples tested, due primarily (but perhaps not exclusively) to its very high Cr content. Finally, the higher system pressures in real sCO_2 systems may be expected to further promote the sulfur-induced corrosion processes revealed herein, and testing at these realistic conditions is recommended prior to deploying a Ni-based alloy for high-temperature service in such environments when sulfur impurities are expected.

Author Contributions R.O. performed characterization and thermodynamic analyses, interpreted the results, prepared the figures, and conceived of and wrote the manuscript. J.T. performed the oxidation experiments. L.T. and C.C. performed additional characterization. O.D. proposed the research and provided guidance throughout the project. All authors contributed to discussion of the results and editing of the manuscript.

Declarations

Conflict of interest The authors declare that they have no known competing financial interests or personal relationships that could have appeared to influence the work reported in this paper.

References

1. K. Brun, P. Friedman, and R. Dennis, *Fundamentals and Applications of Supercritical Carbon Dioxide (sCO$_2$) Based Power Cycles*, (Woodhead Publishing, 2017).
2. R. Allam, et al., *Energy Procedia* **114**, 5948 (2017).
3. R. P. Oleksak and F. Rouillard, Materials performance in CO$_2$ and supercritical CO$_2$. in *Comprehensive Nuclear Materials*, 2nd ed, eds. R. J. M. Konings and R. E. Stoller (Elsevier, Oxford, 2020), p. 422. https://doi.org/10.1016/B978-0-12-803581-8.11622-4
4. R. P. Oleksak, G. R. Holcomb, S. Carney, and Ö. N. Doğan, *Corrosion Science* **206**, 110488 (2022).
5. B. A. Pint, R. Pillai, M. J. Lance, and J. R. Keiser, *Oxidation of Metals* **94**, 505 (2020).
6. R. P. Oleksak, J. H. Tylczak, G. R. Holcomb, and Ö. N. Doğan, *Corrosion Science* **157**, 20 (2019).
7. B. A. Pint, R. G. Brese, and J. R. Keiser, The Effect of Impurities and Pressure on Oxidation in CO$_2$ at 700°–800 °C, in *2018 NACE CORROSION Conference* (NACE International, Phoenix).

8. P. Huczkowski, D. J. Young, T. Olszewski, A. Chyrkin, and W. J. Quadakkers, *Oxidation of Metals* **89**, 651 (2018).

9. N. Mu, K. Y. Jung, N. M. Yanar, G. H. Meier, F. S. Pettit, and G. R. Holcomb, *Oxidation of Metals* **78**, 221 (2012).

10. J. Mahaffey, et al., *Metallurgical and Materials Transactions A* **49**, 3703 (2018).

11. J. Mahaffey, D. Adam, A. Brittan, M. Anderson, and K. Sridharan, *Oxidation of Metals* **86**, 567 (2016).

12. J. Lehmusto, J. Kurley, M. Lance, J. Keiser, and B. A. Pint, *Oxidation of Metals* **94**, 95 (2020).

13. B. A. Pint, J. Lehmusto, M. J. Lance, and J. R. Keiser, *Materials and Corrosion* **70**, 1400 (2019).

14. K. Li, Y. Zeng, and J.-L. Luo, *Corrosion Science* **184**, 109350 (2021).

15. J. P. Shingledecker, S. C. Kung, and I. G. Wright, *Predicting the Oxidation/Corrosion Performance of Structural Alloys in Supercritical CO₂*, (Electric Power Research Institute, 2017), p. 1.

16. R. P. Oleksak, C. S. Carney, and Ö. N. Doğan, *Corrosion Science* **215**, 111055 (2023).

17. R. P. Oleksak, J. H. Tylczak, C. S. Carney, G. R. Holcomb, and Ö. N. Doğan, *JOM Journal of the Minerals Metals and Materials Society* **70**, 1527 (2018).

18. R. P. Oleksak, J. H. Tylczak, G. R. Holcomb, and O. N. Dogan, *JOM Journal of the Minerals Metals and Materials Society* **72**, 1822 (2020).

19. M. Stroosnijder and W. Quadakkers, *High Temperature Technology* **4**, 141 (1986).

20. F. Gesmundo, D. Young, and S. Roy, *High Temperature Materials and Processes* **8**, 149 (1989).

21. H. J. Grabke, R. Lobnig, and P. Papaiacovou, Mechanisms of oxidation and sulfidation of high temperature alloys in H2-H2O-H2S mixtures. in *Selected Topics in High Temperature Chemistry: Defect Chemistry of Solids*, eds. Ø. Johannesen and A. G. Andersen (Elsevier, New York, 1989), p. 1989.

22. J. Stringer, Mixed oxidant corrosion in coal combustion and conversion systems: manifestations and mechanisms, in *High-Temperature Oxidation and Sulphidation Processes* (Elsevier, 1990), p. 257.

23. T. Gheno and B. Gleeson, *Oxidation of Metals* **84**, 567 (2015).

24. B. Grégoire, X. Montero, M. C. Galetz, G. Bonnet, and F. Pedraza, *Corrosion Science* **155**, 134 (2019).

25. R. P. Oleksak, C. S. Carney, G. R. Holcomb, and Ö. N. Doğan, *Oxidation of Metals* **90**, 27 (2017).

26. R. P. Oleksak, M. Kapoor, D. E. Perea, G. R. Holcomb, and Ö. N. Doğan, *NPJ Materials Degradation* **2**, 25 (2018).

27. A. Chyrkin, P. Huczkowski, V. Shemet, L. Singheiser, and W. J. Quadakkers, *Oxidation of Metals* **75**, 143 (2011).

28. D. Caplan and G. Sproule, *Oxidation of Metals* **9**, 459 (1975).

29. J. H. Chen, P. M. Rogers, and J. A. Little, *Oxidation of Metals* **47**, 381 (1997).

30. B. Gleeson, *Materials Research* **7**, 61 (2004).

31. R. Peraldi, D. Monceau, and B. Pieraggi, *Oxidation of Metals* **58**, 275 (2002).

32. C. Sha, L. Yang, J. M. Cairney, J. Zhang, and D. J. Young, *Corrosion Science* **222**, 111410 (2023).

33. M. C. Pope and N. Birks, *Oxidation of Metals* **12**, 173 (1978).

34. N. Birks, Corrosion mechanisms of metals and alloys in multicomponent oxidative environments, in *Symposium on Properties of High Temperature Alloys with Emphasis on Environmental Effects, Las Vegas, NV, USA*, eds. Z. A. Foroulis and F. S. Pettit (Electrochemical Society), p. 215.

35. S.-H. Choi and J. Stringer, *Materials Science and Engineering* **87**, 237 (1987).

36. Z.-S. Liu, W.-K. Li, and M.-J. Hung, *Journal of the Air & Waste Management Association* **64**, 1038 (2014).

37. B. Li and C. Ma, *Energy Procedia* **153**, 471 (2018).

38. M. H. LaBranche and G. J. Yurek, *Oxidation of Metals* **28**, 73 (1987).